Super Lyot ExoEarth Coronagraph (SLEEC)

NASA Strategic Astrophysics Technology Program

Final Report

Principal Investigator: John Trauger

Co-Investigators: Pin Chen, John Krist, Dwight Moody

7 January 2025

Jet Propulsion Laboratory
California Institute of Technology

Signature Page

E-SIGNED by John Trauger
on 2025-09-19 00:38:04 GMT

John Trauger Date

Principal Investigator

E-SIGNED by Brendan Crill
on 2025-09-18 21:32:54 GMT

Brendan Crill Date

Deputy Program Chief Technologist, ExEP

E-SIGNED by Nicholas Siegler
on 2025-09-18 21:33:13 GMT

Nick Siegler Date

Program Chief Technologist, ExEP

E-SIGNED by Lucas Paganini
on 2025-09-19 14:52:28 GMT

Lucas Paganini Date

ExEP Program Executive, NASA HQ

Super Lyot ExoEarth Coronagraph (SLEEC)
Final Report

Table of Contents

Super Lyot ExoEarth Coronagraph (SLEEC)

Final Report

Introduction

The objective of the SLEEC design and testbed experiments is the validation of coronagraph models for high contrast imaging from a space observatory. Validated models are required as bedrock guidance for the design of an HWO space observatory operating at contrast levels adequate for the imaging and spectroscopy of earth-sized exoplanet systems in reflected starlight. The SLEEC design presented here (***Appendix A***) achieves HWO levels of contrast and throughput. The outstanding challenge for this work was (and remains) the implementation of testbed hardware with sufficient perfection to test coronagraph performance at 10^{-10} or better contrast levels (see ***Appendices B&C***). For this SAT program, we rely on the Decadal Survey Testbed (DST) facility, provided by the Exoplanet Exploration Program (ExEP), which defines the achievable levels of validation.

The SLEEC demonstrations described here focus on the performance of the hybrid Lyot coronagraph (HLC). Versions of the classic and hybrid Lyot coronagraph have consistently demonstrated 4-6 x10^{-10} normalized intensity (dark field contrast) over a 10% spectral bandwidth in the laboratory (Trauger et al., 2011; Seo et al., 2019; Crill, 2022). The HLC is the primary coronagraph mode for imaging demonstrations in the Roman CGI (Trauger et al., 2016; Kasdin et al., 2020). HLC was identified among the leading coronagraph options for HabEx and LUVOIR (Gaudi et al., 2020; LUVOIR team, 2019).

The Decadal Survey Testbed employed a classical Lyot coronagraph for its initial commissioning demonstration. That experiment yielded a contrast of 4x10^{-10} over a 10% spectral bandwidth in a 360° field of view extending from 3 to 10 λ_0/D. A handful of testbed characteristics limiting the DST contrast performance were identified by the commissioning team (Seo et al., 2019, 'S19' hereafter), each estimated to increase the background and diminish contrast in increments of ~10^{-10} in the commissioning demonstrations.

SLEEC's objective is the design and demonstration of a higher performing coronagraph, as judged in terms of contrast, throughput, and practical considerations such as error tolerance and feasibility of manufacture. In past design studies, we have used conventional, gradient-based optimization algorithms. These evolve the state of design parameters such that it descends a local least-squares valley of the performance metric surface. These design algorithms do not search for the global optimum, and the obtained solution may be a sub-optimal local minimum particular to the initial state. Initial SLEEC investigations focused on a global search for a high performing coronagraph architecture with a minimum number of free design parameters, as described in ***Appendix D***. As these architectures are typically limited to contrast levels around 10^{-5}–10^{-6}, they were envisioned as the initial state for further design refinements and wavefront control with deformable mirrors. Prolate spheroidal waveforms were identified as the ideal basis for the purpose of concentrating energy centrally on the focal plane mask. However, deformable mirrors are more generally able to direct energy elsewhere, including outside the periphery of the Lyot stop. Accordingly, we also pursued a heuristic design approach guided by past testbed experience and practical considerations of focal plane mask fabrication.

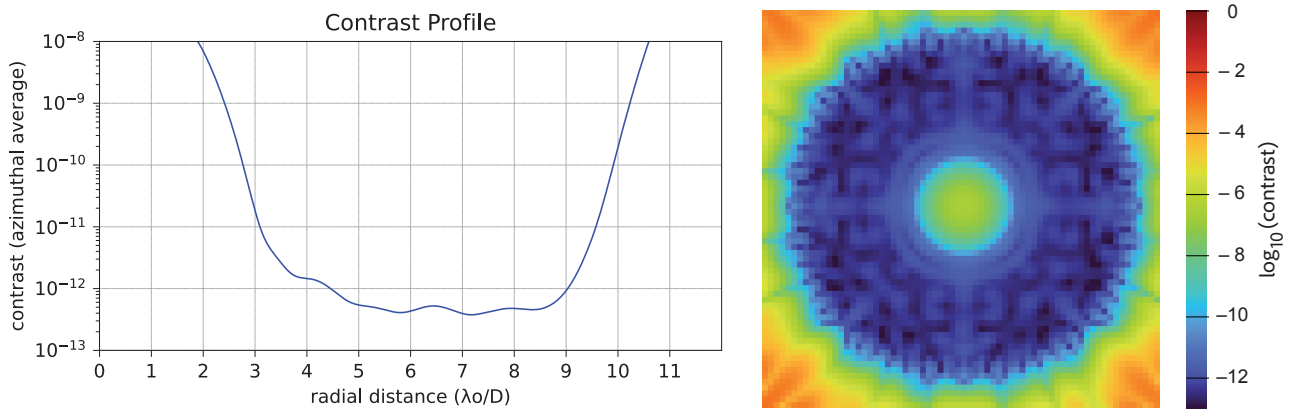

Figure 1. Image contrast computed for the SLEEC hybrid focal plane mask. At left is the azimuthally averaged dark-field intensity. Contrast averages ~5x10^{-13} in the 360° dark field extending from 3 to 9 λ_0/D with a 10% bandwidth centered at λ_0 = 550 nm wavelength. "Core throughput" in the high contrast dark field is 18% (encircled energy within a contour drawn at half peak intensity of the PSF), to be compared with a core throughput of 49% for the PSF of an unobscured telescope alone. Hence 0.18 / 0.49 = 37% of theoretical exoplanet photons propagating with perfect optics from the telescope to the coronagraph will appear for detection in the high contrast dark field.

We developed a new hybrid Lyot focal plane mask (FPM) designed to meet the requirements featured in the ExEP Technology Gap List: contrast better than $1x10^{-10}$ in a dark field with an inner working angle (IWA) of 3 λ_0/D at visible wavelengths, over a 10% spectral bandwidth, with core throughput greater than 10% (Crill, 2022). Theoretical models of the SLEEC coronagraph performance predict contrast of ~$5x10^{-13}$ averaged across a 360° high contrast dark field extending from 3 to 9 λ_0/D with a 10% spectral bandwidth centered at λ_0 = 550 nm wavelength, as indicated in Figure 1 and described further in ***Appendix A***. To provide a close comparison with past DST experience, the SLEEC experiments also included a classic Lyot mask with a simple circular opaque occulting spot, which is calculated to reach contrast levels of ~10^{-10} over the same dark field and bandwidth.

The SLEEC FPM is designed with simplicity of manufacture in mind. The Lyot type coronagraph is among the least complex candidate technologies for 10^{-10} contrast demonstrations. The SLEEC FPM comprises standard well-characterized optical thin-film materials (nickel, cryolite, magnesium fluoride) deposited on a fused silica substrate of the highest commercial quality. It can be made by either vacuum deposition through stencil masks (in JPL facilities) or by conventional lithography techniques, as described in ***Appendix A***. Simplicity of design and use of standard materials enables precise prediction and verification of the FPM's optical characteristics. These focal plane masks are inherently insensitive to the polarization state of the light.

A coronagraph operating at high contrast places stringent requirements on wavefront control and testbed stability. In general, contrast levels better than 10^{-10} require wavefront control at the ~1-10 picometers rms level (Traub and Oppenheimer 2010; Burrows 2005). The high contrast dark field is created by, and its extent and depth defined by specific surface patterns on a pair of deformable mirrors. Sensitivities to actuator noise and low order wavefront errors are discussed in ***Appendix A***. Wavefront control at the required levels is among the most challenging aspects of these demonstrations.

DST experiments

HLC architecture is among the simplest possible for a high contrast coronagraph, with only one transmissive element – a focal plane mask formed on a high-quality fused silica glass substrate – and a minimum of other complications (no other transmissive or polarizing elements in the highly corrected wavefront upstream of the Lyot stop). This simplifies and improves confidence in the performance modeling and the estimation of tolerances to manufacturing imperfections.

Our objective was to demonstrate contrast performance matching the theoretical predictions to the extent possible, and to probe and understand the apparent causes of any deviations from the theoretical predictions. As indicated below, the demonstrated contrast was limited by scattered light and other factors in the DST itself. However, an empirical investigation of the origins of incoherent background light in the DST proved to be beyond the scope of support for SAT programs. The DST is a shared facility, which makes one-time testbed modifications or adjustments on behalf of individual SAT investigators either challenging or infeasible. Instead, we use information gleaned from the experiments to speculate on the likely sources of scattered background light – but without the opportunity to test these speculations by tweaking and adjusting the alignment of the DST optics or by visually searching for sources of stray light.

Each of eleven SLEEC experiments was carried out with the baseline DST optical layout with the addition of various focal plane masks and Lyot stops. Each demonstration involved 100 iterations of electric field conjugation (EFC) with the FALCO software package, with the specific goal of best contrast averaged from 3-9 λ_0/D. The DST experiment operator used the FALCO package to optimize actuator settings on a pair of DMs for a 360° dark field (as proposed) and the alternative of using both DMs for a 180° half dark field (as a diagnostic).

The high-contrast dark fields were dominated by ghost background speckles at contrast levels of $5.2\pm1.0 \times 10^{-10}$. The distribution of background speckle features appeared uncorrelated from one experiment to the next, and the presence of random background features obscured estimates of focal plane mask performance. We highlight four of the eleven experiments carried out on the DST. These four were selected to distill what can be learned about SLEEC focal plane mask performance.

Analysis of the DST data

We take advantage an important feature of the iterative pairwise probing EFC procedure for optimization of the DST deformable mirror settings – which naturally distinguishes between those components in the image that are modulated by the probing patterns on the DM, and the residual background components which are unmodulated by the probing patterns – and which is reported for each iteration by the controlling FALCO software. Commonly referred to as the ‘coherent’ and ‘incoherent’ components, these are

respectively the components that respond as expected to EFC probing (the modulated signal) and the components that are unaffected by EFC probing (the unmodulated signal).

DST results may be modeled in terms of a contrast floor with the addition of incoherent ghost images and scattered light. The coherent component in the coronagraph images is modeled in terms of an optically perfect DST with various focal plane masks and Lyot stops, as outlined in ***Appendix A***. Incoherent ghost features and scattered light are not susceptible to modeling due to lack of sufficiently detailed knowledge of the elements in the DST optical path. Instead, we distinguish between characteristics of the coherent and incoherent components in the images, seeking further insight into their origins.

Figure 2 is a template for display of the coherent and incoherent components in the images in each of the five 2% bands, as well as the total composite image (without discrimination between coherent and incoherent) across the full 10% band, all with a linear contrast stretch.

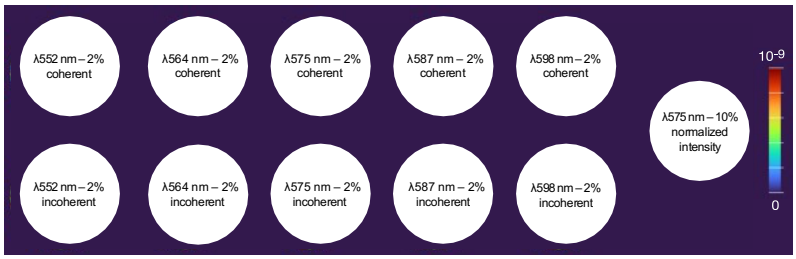

Figure 2. Template for the following discussion.

An analysis of the 2% images was performed, in which the pixels were binned in circular patches of diameter 1.5 λ_0/D on a square sample grid spaced by 0.5 λ_0/D. This "speckle binning" is intended to filter the image for intensity features on the approximate scale of a speckle in the coronagraph image. Results of this binning are not sensitive to the precise choices of diameter and pitch of the sample patches. Median intensities are posted for each distribution and, as a check for consistency, the contrast averaged over the 10% dark field is quoted for comparison with the FALCO score.

A set of three histograms accompanies each data set. Histograms of the contrast averaged over these patches are plotted separately for the coherent and incoherent components in the 2% bandpass centered on λ_0, and for the total intensity averaged over the 10% bandpass. A picture emerges in which the (coherent) contrast floor falls generally in the ~1×10^{-10} range. We interpret this component as indicative of the underlying true contrast floor, i.e., the contrast performance that would be achieved in the absence of scattered light and other testbed factors in the DST not included in the optical models. Meanwhile, ghost and scattered light (incoherent) features appear in successive experiments with variable random intensities distributed over random locations, which we interpret as originating from variations from one experiment to the next in internal reflections, scattered light, and other uncertainties in the DST, as further discussed in ***Appendices B and C***.

Experiment B.1. Classic Lyot FPM (DST commissioning mask)

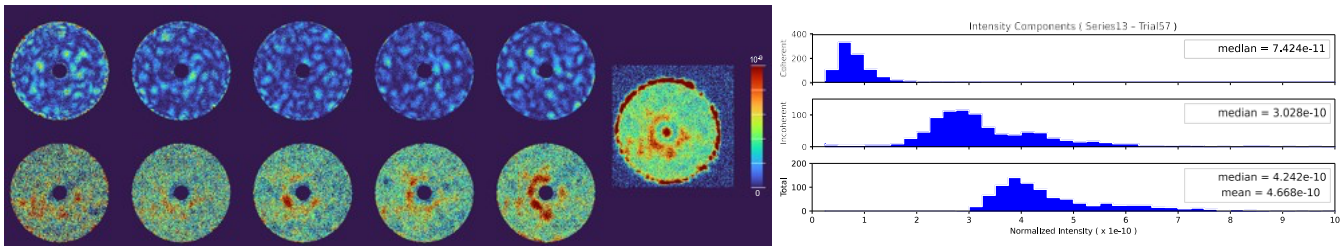

B.1, Series 13, Trial 57 (with polarization analyzer)

Experiment B.1. This experiment repeats the nominal configuration for the DST commissioning experiment carried out by Seo et al. (S19). It was intended to establish a DST performance baseline, against which to judge any improvements in performance of the SLEEC FPMs. The configuration includes the original commissioning classic Lyot FPM and an annular Lyot stop, solving for a 360° dark field extending from 3 to 9 λ_0/D in 10% bandwidth light centered at λ_0 = 575 nm. The contrast score reported by the FALCO package is 6.1×10^{-10} without polarization analyzer, which improved to 4.7×10^{-10} with the addition of a linear polarizing analyzer downstream of the coronagraph. The contrast computed by the binning technique described above and shown in the histogram is 4.7×10^{-10} for the case with polarizer in place, in good agreement with the FALCO estimate.

This result is comparable to the results of Seo et al. (S19), who reported a contrast of 3.8×10^{-10} averaged over a 360° dark field extending from 3 to 8 λ_0/D in 10% bandwidth light centered at 550 nm, also with a linear polarizing analyzer in place. However, as discussed by Seo et al., comparison with a theoretical prediction of 1.2×10^{-10} contrast indicates the presence of ~4×10^{-10} in additional background light, which was attributed to the least-significant-bit (LSB) voltage discretization in the DM driver electronics, chromatic effects in the FPM, ghost images, testbed jitter, and otherwise unknown sources.

While the theoretical contrast for the SLEEC design is better than the classic Lyot commissioning design by orders of magnitude, any potential improvements in testbed performance are obscured by relatively large speckle features in the high contrast field that are variable from one experimental setup to the next. The contrast improvement predicted for the SLEEC FPMs cannot be reliably demonstrated without a solid baseline contrast that is understood and repeatable within 10^{-10} or better. Which leads to the next highlighted experiment.

Experiment B.2. Classic Lyot FPM (DST commissioning mask) repeated

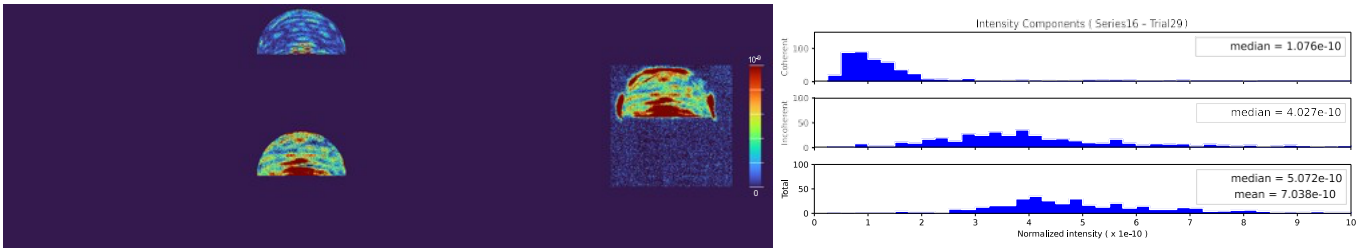

B.2, Series 16, Trial 29

Experiment B.2 (Series 16, Trial 29). This result is highlighted because it is the only repeat experiment with the DST commissioning mask carried out for the SLEEC project. This is our only direct test of repeatability in the DST experiments. FALCO score for contrast is 7.5×10^{-10}, which is in close agreement with the 7.0×10^{-10} contrast estimated with the binning technique and shown in the histogram. Median intensities of the coherent and incoherent components are comparable to **B.1**, while the mean total intensity is skewed by bright features that are not present in **B.1**. Inspection of the images shows that the morphology in the incoherent light is quite different.

What has changed between these experiments? The FPM has been demounted and remounted with unmeasured and likely different tilts. The intended circular Lyot stop with diameter 69% of the pupil was used, while the previous experiment used the annular commissioning Lyot stop. Tilt and reflective properties of the Lyot stops were not measured. This experiment used two DMs to create a 180° half dark field. Only the central 2% band was included. The difference in the unmodulated speckle backgrounds in **B.1** and **B.2** cannot be attributed to the FPM itself, which is unchanged. It must be attributed to unmeasured differences in the tilts of the FPMs and Lyot stops, and to differences in reflective characteristics of the Lyot stops.

However, the median intensities appear to be repeatable and, particularly, the coherent component is near the 1.2×10^{-10} contrast predicted in Dwight Moody's theoretical model for the hard-edged classic Lyot FPM (see ***Appendix A***).

We conclude that the coherent component, as estimated by the binning technique, is our most reliable indicator of FPM performance in the SLEEC DST experiments.

Experiments B.10 & B.11. SLEEC hybrid Lyot FPM (manufactured by SILIOS)

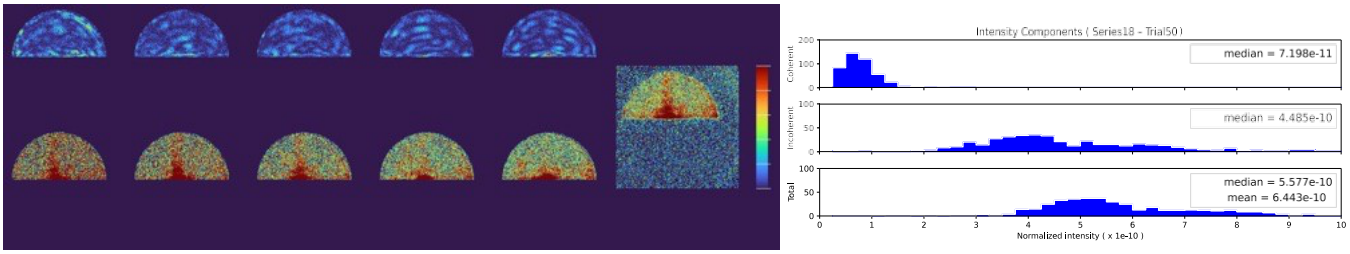

B.10, Series 18, Trial 50

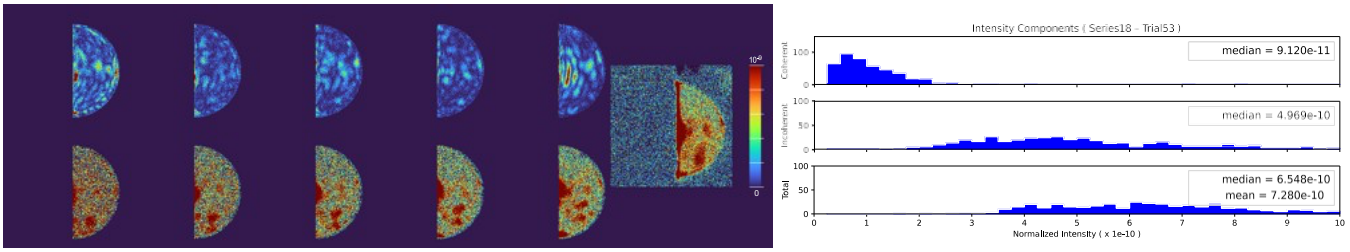

B. 1, Series 18, Trial 53

Experiments B.10 and B.11 are highlighted as demonstrations of the SLEEC focal plane mask. As described in Section A.1.1, this FPM was formed on a plane parallel fused silica substrate with conventional lithographic techniques by SILIOS. Substrate thickness is 6.4 mm, anti-reflection coated on the backside. Tilt of the FPM in this experiment was measured to be 6° by locating the beam reflected by the FPM. This tilt offsets the internally reflected ghost reflections away from the dark field. The Lyot stop is an unobscured circular aperture with diameter 69% of the pupil diameter, close to the optimal design 70% diameter. The DST experiment operator chose to optimize the DM settings for best contrast over a 180° half dark field across the 10% spectral band centered at 575 nm. The DST setup was unchanged between the experiments, except for the selection of different D-shaped 180° field stops for the 'north' half field (Series 18, Trial 50) and the 'east' half field (Series 18, Trial 53).

The median dark field intensities in coherent light are 7.2x10^{-11} and 9.1x10^{-11} respectively, while the median incoherent component is ~5x10^{-10}. FALCO scores were 4.6x10^{-10} and 5.6x10^{-10} respectively for contrast averaged across the 10% spectral band.

Summary of the SLEEC experiments

Experiments were carried out by the DST experiment operator with various combinations of focal plane masks, Lyot stops, and field stops. Overall, they have demonstrated total contrast (coherent + incoherent) at levels between 3-7x10^{-10} in a 10% spectral bandwidth centered on 575 nm wavelength. None of these demonstrated the theoretically predicted contrast illustrated in ***Figure 1***. The four examples above were selected as representative of these DST experiments, with results collected in ***Table 1***.

	Focal Plane Mask	Lyot Mask	BW	FOV	median coherent x10^{-10}	median incoherent x10^{-10}	median total x10^{-10}	FALCO score x10^{-10}
B.1	Classic - DST	DST	10%	360°	0.74	3.02	4.67	4.7
B.2	Classic - DST	0.69 D	2%	180°	1.08	4.03	5.07	7.5
B.3	Classic - DST	0.69 D	2%	180°	0.87	4.61	5.54	8.3
B.10	SLEEC - Silios	0.69 D	10%	180°	0.72	4.49	5.58	4.6
B.11	SLEEC - Silios	0.69 D	10%	180°	0.91	4.97	6.55	5.6

Table 1. We have selected these results as representative of a total of eleven experiments carried out by the testbed operator on the DST. The "Classic-DST" FPM is the same mask that was used in DST commissioning, as described in ***Appendix A.2***. The "SLEEC-Silios" FPM was designed and manufactured as part of this SAT project, as described in ***Appendix A.1***. Median coherent and incoherent components of the contrast over the 3-9 λ_0/D field are calculated by the speckle binning method. The FALCO score is the normalized intensity (contrast) averaged over 3-9 λ_0/D computed by the FALCO software and as typically reported for DST results.

The overall results were consistent in the sense that ***coherent contrast***, as estimated by the speckle binning technique, was generally near or better than 10^{-10} in all eleven experiments, while morphology of the ***incoherent background*** was capriciously variable from one experiment to the next, and generally at levels of $4x10^{-10}$ or greater. We believe that the changes observed in background morphology are the likely result of capricious and unmeasured variations in the alignments (tilts) in the critical focal plane and Lyot elements, as indicated in ***Appendix B***. ***Again, we conclude that the coherent component, as estimated by the binning technique, is our most reliable indicator of FPM performance in the SLEEC DST experiments.*** The results indicate that contrast better than 10^{-10} is achievable with the SLEEC focal plane mask design, but that robust experimental demonstrations to that effect will require further efforts in control of background reflected and scattered light in the testbed, with emphasis on the items in ***Appendix C***.

Milestones

The SLEEC milestones are defined in the White Paper (Trauger et al. 2018). The programmatic environment for this study have evolved significantly since the WP was written. At that time that the Decadal Survey Testbed (DST) had been recently commissioned and the LUVOIR final report was still in draft form. Year-long delays in laboratory fabrication activities at JPL were mandated by COVID restrictions. Access to the DST was likewise delayed due to COVID restrictions and during a period of dedicated support to the Roman CGI project. Further, the new Habitable Worlds Observatory has supplanted HabEx and LUVOIR as the fiducial flagship exoplanet mission concept. Nevertheless, the SLEEC objectives remain fresh, challenging, and directly relevant to the new HWO initiatives. The SLEEC milestones are as follows:

Milestone 1a (M1a). "Design a Lyot-type coronagraph for a HabEx unobscured off-axis telescope with raw contrast of 10^{-10} or better for spectral bandwidths ≥ 10%, with tolerances to expected levels of telescope jitter and low-order thermal drifts." As summarized in this report, a SLEEC design with theoretical contrast better than 10^{-12} and core throughput of 18% over a 10% bandwidth meets and exceeds the ***M1a*** and ExEP contrast and throughput requirements (Crill 2022). Prototype masks have been successfully fabricated both in the JPL laboratory and with conventional lithographic techniques by a commercial vendor (Silios).

Milestone 1b (M1b). "Using the ***M1a*** coronagraph elements on the newly commissioned ExEP Decadal Survey Testbed (DST), demonstrate 10^{-10} contrast, 10% bandwidth in a simulated static vacuum lab environment, IWA = 3 λ/D." The DST experiments summarized here have demonstrated total contrast (coherent + incoherent) at levels between $3\text{-}7x10^{-10}$ in a 10% spectral bandwidth centered on 575 nm wavelength. None of the experiments demonstrated the theoretically predicted contrast illustrated in ***Figure 1***. The challenges of high contrast laboratory demonstrations were anticipated and are well documented, and we conclude that further testbed refinements are needed (***Appendix C***) before ***M1b*** can be successfully demonstrated. We also note that the testbed refinements listed in the Appendix are among the objectives of a new SAT 2022 study which is focused on low order wavefront control with the dedicated Compact Coronagraph in the PI's laboratory (Trauger et. al. 2024a & 2024b).

Milestone 2a (M2a). "Design a Lyot-type coronagraph for the LUVOIR telescope with a segmented primary mirror configuration as defined by the LUVOIR team. Once the LUVOIR configuration has been defined (as expected during the first year of this study), then we will seek the best exoplanet performance." Initial investigations in search of a global coronagraph design approach were carried out for the LUVOIR aperture (***Appendix D***). However, success of the LUVOIR coronagraph is critically sensitive to details of the segmented telescope primary mirror, including surface figure and stability of the individual segments; inter-segment wavefront phase control and stability; effective size of the inter-segment gaps, and secondary mirror obscurations. The ***M1a*** SLEEC mask can be considered a candidate for an idealized LUVOIR with wavefront perfection and stability. But a meaningful test of the design critically requires deeper engineering knowledge of the segmented primary mirror and optical systems. Such engineering studies are being taken up by the HWO project, and will be key requirement for realistic coronagraph designs.

Milestone 2b (M2b). "The manufacture and demonstration of the ***M2a*** coronagraph elements on the newly commissioned DST. Expected performance levels will be determined during the design phase of M2a." A meaningful DST experiment for the segmented telescope requires a high-fidelity testbed simulation of a multi-segment pupil. The implementation of a segmented mirror testbed is a priority in ExEP planning for future development of the DST.

Lessons learned

Our objective has been to identify and quantify (to the extent possible with available testbed data) the extent of agreement as well as possible sources of discrepancy between theoretical expectations and the experimental performance. Here are six lessons learned in the SLEEC experience.

(1) ***The DST is itself a critical part of this experiment***. These experiments have demonstrated total contrast (coherent + incoherent) at levels between 3-7x10^{-10} in a 10% spectral bandwidth centered on 575 nm wavelength. None of these demonstrated the theoretically predicted contrast illustrated in ***Figure 1***. While our objective is the laboratory validation of theoretical predictions, it was known in advance (from the DST commissioning demonstrations) that it would be necessary to reduce and/or understand and stabilize any factors in the DST testbed that introduce incoherent background light at ~10^{-10} contrast levels**.**

Greater suppression of the incoherent and scattered background in the DST is necessary to validate model predictions of SLEEC contrast performance. A list of potential sources of unwanted background is collected in ***Appendix C***. To the extent possible, these sources must either be reduced to insignificance (compared to the ExEP Gap List requirement of 10^{-10} contrast) or be identified, understood, and validated to ~10^{-10} levels or better. A significant investment in time and resources will be required to understand and mitigate these sources.

(2) ***It is evident that incoherent background is dominant in the DST coronagraph images, with capricious variability from one experiment to the next and with intensities generally greater than the coherent components.***

The DST experiments illustrate that contrast in the ***coherent components*** of the dark field images are consistently better than ~1x10^{-10}, while the ***incoherent components*** are generally in the range of 4x10^{-10} and greater. This behavior is a signature of incoherent ghost images created by near-normal internal reflections in the DST coronagraph optical path, as discussed in ***Appendix B***.

(3) The ***demonstrated coherent-light contrasts*** for the classic Lyot and SLEEC coronagraph FPMs suggest that these designs are performing near or slightly better than 10^{-10} contrast levels in coherent light. Results are tabulated in ***Table 1***. A definitive first step towards demonstrations of performance that closely match the theoretical predictions requires a significant reduction or quantitative explanation of the potential sources of incoherent background in the DST (***Appendix C***). The identification and mitigation of dominant sources of incoherent background must be a high priority in future DST experiments.

(4) ***Scattered background light***. The variation in patterns of incoherent background between one DST run and the next can be explained in terms of alignments, tilts, and properties of shiny coronagraph elements. Consider these examples with the DST commissioning FPM.

- Experiment B.1 is a repeat of the DST commissioning experiment with contrast score of 4.6x10^{-10} in the full 360° field, 10% bandwidth, in this case with the annular DST commissioning Lyot stop (annular stop is illustrated in Appendix A.2).
- Experiments B.2 and B.3 were carried out later with the same FPM but instead using a circular Lyot stop with radius 0.69 *D*, giving contrast scores of 7.5x10^{-10} and 8.4x10^{-10} over 180° fields with 2% bandwidth.
- Inspection of the images in B.1, 2, and 3 shows that the coherent components in the images are comparable with contrast <~10^{-10}, while the incoherent patterns are quite different. Further, better contrast would be expected for the half-dark-field and 2% bandwidth in the B.2 and B.3 experiments, but instead it is somewhat worse.

What changed? Same FPM, but the FPM was remounted between B.1 and B.2,3 and likely has a different tilt. The Lyot stops were exchanged and the reflecting properties and tilts of these shiny foil masks are likely different. All else is unchanged in the DST. We posit that the changes in incoherent background can be explained as rearrangements of ghost images from one experiment to the next, with a rationale given in ***Appendix B***. This hypothesis could be tested by experimentally varying the tilt of each of the five reflective DST elements identified in ***Figure B1***. However, such tinkering with alignments was not feasible given the programmatic constraints on DST experiments.

(5) ***Particulate contamination*** is not a significant factor in the results. As shown in ***Appendix A***, the FPMs were inspected for particulates in the PI's laboratory following the experiments. Microscope images indicate a sparse population of particulates less than 2 μm in size, near the resolution limit of the microscope. As outlined in the Appendix, a model of the iterative EFC procedure for DM settings, implemented in the FALCO package, in which a single particulate is added to the standard FPM pattern indicates that static particulates of this size have no significant effect on the coronagraph contrast at the ~10^{-12} level.

(6) ***Incoherent polarization cross terms*** have been a consistent and unexplained presence in the JPL testbeds over the past years. The DST light source is circularly polarized. Polarized light is implicated in experiment B.1, which was carried out with (4.6x10^{-10}) and without (6.1x10^{-10}) a linear polarization analyzer at the end of the optical path. The Lyot coronagraph is in principle insensitive to polarization states. Incoherent polarized light is likely the signature of glints or other scattering mechanisms in the DST optical path. Analysis is needed to identify the polarization effects, which is an important factor in all coronagraph experiments at contrast levels better than 10^{-10} on the DST.

Conclusions

An investigation of DST performance limits near the 10^{-10} contrast levels could be carried out in demonstrations with the classic Lyot coronagraph, which in its simplicity is a test not of the coronagraph design but rather of the potential testbed factors in ***Appendix C***. An established baseline with the classic Lyot coronagraph, in which coronagraph performance improvements have been quantified in increments of 10^{-10} contrast or better, is required before we can begin to verify the predicted benefits of the SLEEC design. Even better, we suggest that such DST performance verifications could be performed to 10^{-11} contrast levels with the SLEEC FPM described in this report.

We understand that the DST, as a configuration-controlled facility that is fully subscribed in service to the broad exoplanet exploration community, is not ideally positioned for schedule-disrupting investigations and refinements of testbed performance. As an alternative, focused investigations could be carried out in small dedicated 'incubator' facilities such as, for example, the compact coronagraph testbed and vacuum chamber in the PI's laboratory. A small facility, narrowly focused on just one issue at a time, could support agile experimentation and incremental refinements of the individual hardware elements and operating procedures. Lessons learned off-line would be highly relevant to the DST efforts, potentially to the benefit of future demonstrations in the DST.

Our work with the SLEEC focal plane mask will continue in the context of a NASA Strategic Astrophysics Technology 2022 program titled "Low Order Wavefront Sensing and Control for Exoplanet Imaging" (Trauger et al. 2024a & 2024b). Here the objective is the implementation and closed-loop demonstration of a new optical element for the active correction of low-order wavefront errors, to be tested in a high contrast Lyot coronagraph with a Zernike wavefront sensor in a laboratory vacuum environment. Wavefront control is separated into active low-order and stable high-order wavefront control elements. This SAT program intends to validate the approach for control and stabilization of low-order wavefront errors characteristic of a large telescope in the space environment. While our emphasis is shifted to the challenge of precision low-order wavefront control for exoplanet imaging, this new SAT project also provides an excellent opportunity to investigate and address the testbed items in ***Appendix C***.

Acknowledgement

With thanks to the Exoplanet Exploration office for support and access to the Decadal Survey Testbed facilities, and to the ExEP Technology Assessment Committee for their review of this report. The research reported here was carried out at the Jet Propulsion Laboratory, California Institute of Technology, under a contract with the National Aeronautics and Space Administration

References

K. Balasubramanian et al. 2019. "Critical characteristics of coronagraph masks influencing high contrast performance." SPIE, doi.org/10.1117/12.2530825.

C. Burrows, 2005. "Effect of actuator flutter on contrast." Personal communication.

B. Crill, 2022. "Progress in Technology for Exoplanet Missions, an Appendix to the NASA Exoplanet Exploration Program Technology Plan." JPL Document D-108825, https://exoplanets.nasa.gov/exep/resources/documents/.

B. Gaudi et al., 2020. "The Habitable Exoplanet Observatory (HabEx) Mission Concept Study Final Report." doi.org/10.48550/arXiv.2002.06683.

N.J. Kasdin et al. 2020. "The Nancy Grace Roman Space Telescope Coronagraph Instrument (CGI) Technology Demonstration." SPIE, doi.org/10.1117/12.2562997.

J. Krist, B. Nemati, B. Mennesson 2016. "Numerical modeling of the proposed WFIRST-AFTA coronagraphs and their predicted performances." JATIS, doi.org/10.1117/1.JATIS.2.1.011003.

LUVOIR Team, 2019. "The LUVOIR Mission Concept Study Final Report." doi.org/10.48550/arXiv.1912.06219.

B-J. Seo et al., 2019, "Testbed demonstration of high contrast coronagraph imaging in search for Earth-like exoplanets." SPIE, doi.org/10.1117/12.2530033.

E. Sidick et al., 2017. "Optimizing the regularization in broadband wavefront control for the WFIRST coronagraph." SPIE, doi.org/10.1117/12.2274440.

W. Traub and B. Oppenheimer, 2010. "Direct Imaging of Exoplanets." In Exoplanets, edited by S. Seager, University of Arizona Press.

J. Trauger et al., 2011. "A hybrid Lyot coronagraph for the direct imaging and spectroscopy of exoplanet systems: recent results and prospects." SPIE, doi.org/10.1117/12.895032.

J. Trauger et al., 2016. "Hybrid Lyot coronagraph for WFIRST-AFTA: coronagraph design and performance metrics." Journal of Astronomical Telescopes, Instruments, and Systems, doi.org/10.1117/1.JATIS.2.1.011013.

J. Trauger et al. 2018. "Super Lyot ExoEarth Coronagraph (SLEEC), Technology Development for Exoplanet Missions (TDEM) White Paper." http://exoplanets.nasa.gov/internal_resources/842.

J. Trauger et al. 2024a. "Low Order Wavefront Sensing and Control for Exoplanet Imaging, Strategic Astrophysics Technology Program (SAT) White Paper." http://exoplanets.nasa.gov/internal_resources/3035.

J. Trauger et al. 2024b. "A hardware implementation for low-order wavefront sensing and control in exoplanet imaging." Proc. SPIE 130926C, doi.org:/10.1117/12.3020600.

Appendix A

SLEEC coronagraph design and manufacture

A.1. SLEEC hybrid Lyot focal plane mask design. The FPM is comprised of thin terraced layers of nickel and a uniform dielectric layer on a fused silica glass substrate, as illustrated in Figures A1-1 and -2. The design minimizes the phase shift across the transition from the edge of the nickel layers to the unobscured surrounding field. Diameter of the nickel element is 101.6 μm, scaled for a 550 nm center wavelength, 10% spectral bandwidth, and a 3 λ_0/D inner working angle in an f/33 beam. Quality of the FPM substrate requires special consideration, as it is the single transmitting element in the highly-corrected optical wavefront upstream of the Lyot stop. The substrate material is Corning class-0A homogeneous fused silica, either thick or slightly wedged, and AR coated on the backside to suppress and remove reflective ghosts from the beam. FPMs were manufactured both by vacuum deposition through stencil masks at JPL and by standard lithographic methods by SILIOS Technologies (Peynier, France).

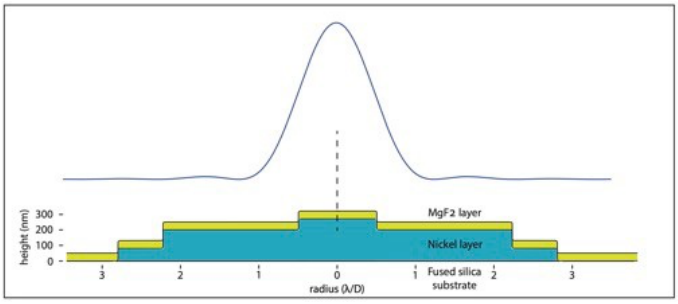

Figure A1-1. Cross section of the SLEEC metal-dielectric focal plane mask consisting of terraced-thickness nickel layers and a uniform-thickness overlayer of magnesium fluoride. The central Zernike phase dimple enables low-order wavefront error sensing. Also shown for scale is the cross section of the Airy point spread function (PSF) at 550 nm wavelength.

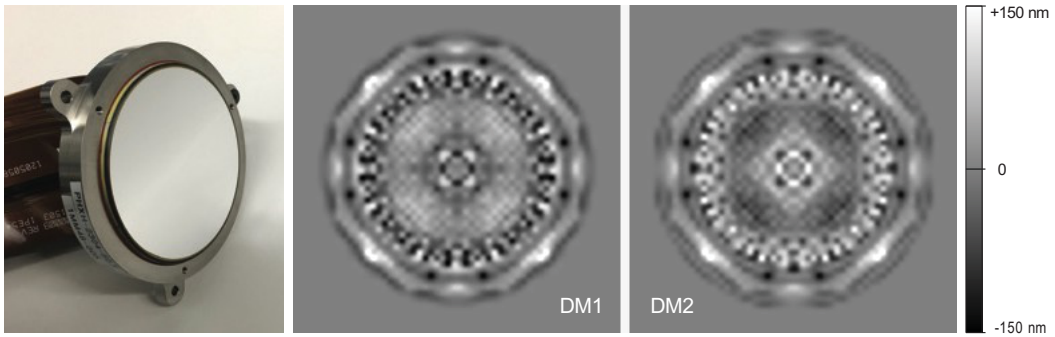

Figure A1-2. The dark field illustrated in ***Figure 1*** is created using a pair of 48x48 actuator deformable mirrors (DMs). Photo at left shows a Xinetics DM with a 48x48 array of PMN actuators spaced on 1x1 mm centers behind a polished fused silica mirror facesheet. At right are the surface figure patterns computed for the SLEEC FPM and an unobscured circular Lyot stop with a diameter of 0.70 x pupil diameter. DM1 and DM2 surface patterns are nominally the inverse of each other inside the 70% diameter of the Lyot stop, and nominally equal outside the 70% diameter. The level of surface deformations amounts to ~50 nm rms across the DMs.

Optimization of the SLEEC design. The essential elements of the SLEEC coronagraph are the FPM shown in Figure *A1-1* and surface shapes imposed on the pair of DMs, one of which is located conjugate to the entrance pupil, and the second located 1 meter downstream in a collimated beam. The circular FPM is opaque to a radius of 2.3 λ_0/D, then steps to a transmittance of 0.006 from 2.24 to 2.8 λ_0/D, then transparent beyond 2.8 λ_0/D. The thicknesses of the superimposed dielectric layer and the outer annular terrace of the FPM were selected to give zero phase shift in transmission at λ_0 across the transition at the outer 2.8 λ_0/D boundary of the FPM. This was observed to improve contrast by more than an order of magnitude compared with the classic Lyot FPM. No further optimizations of the FPM design were tested. The central 'dimple' provides a quarter-wave phase shift in reflection for low-order Zernike wavefront sensing, which is not part of this SAT demonstration.

The surface shapes on the DMs shown in Figure *A1-2* were determined by iteratively solving for a minimum in the cost metric using the FALCO software package. The metric is: $m = (C+\rho) / \eta$, where m is proportional to the integration time to reach a given S/N for exoplanet detection, C is the coronagraph contrast ratio, ρ represents the incoherent background signal in the dark field (ratio of exoplanet and zodi light intensities to the peak starlight intensity) that is not suppressed by the coronagraph, and η is the coronagraph "core throughput." For design purposes, the background signal was set to $\rho = 0$, allowing the algorithm to minimize the (C/η) ratio without penalty for achieving contrast better than an arbitrarily speci5ied background signal.

Core throughput is defined as the fraction of the energy from a star or exoplanet received by a telescope's primary mirror that reaches the instrument focal plane within a contour at the half peak intensity of the PSF (Krist et al. 2016) for perfectly transmitting optics. This definition provides intuitive insight into detectability of the exoplanet against a background of speckle noise in the dark field, an important consideration when comparing coronagraph architectures with irregular or broadly extended PSFs. ***It is not a measure of total energy in the PSF.*** For example, given the Airy PSF characteristic of an unobscured circular telescope aperture, the core throughput is 49%. The SLEEC coronagraph incorporates a circular Lyot mask that obscures the pupil outside 70% of the diameter. Hence the core throughput of the coronagraph with flat DMs reduces to $0.49*0.70^2 = 24\%$.

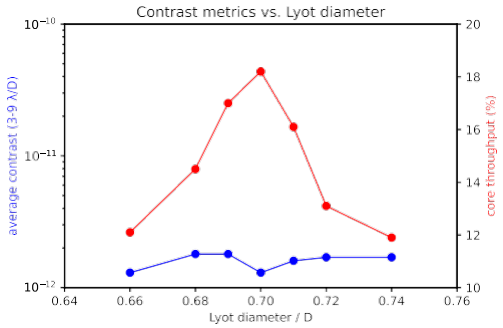

Figure A1-3. FALCO optimizations were carried out for a range of Lyot stop diameters. The figure indicates that contrast (blue) falls consistently below $2x10^{-12}$, while the core throughput (red) reaches a well-defined peak near 18% at a Lyot diameter of 0.7 / *D*. Smaller Lyot apertures directly reduce throughput, while larger Lyot apertures force the DMs to compensate by scattering more light, leading to a declining trend in throughput that dominates beyond the 70% diameter.

FALCO optimizations were carried out for a range of Lyot diameters. The contrast C, averaged over the 3-9 λ_0/D, 360° dark field, consistently reaches a floor better than $2x10^{-12}$. The core throughput η for a typical sequence of ~100 FALCO iterations declines as the DM surface shapes evolve from flat to deformation patterns such as shown in Figure *A1-2*. As seen in Figure *A1-3*, core throughput falls in the 12-18% range for Lyot diameters near 0.70 *D*.

The DM surface shapes generated for the 70% Lyot stop result in a core throughput of 18.2%. ***Measured in terms of core throughput, the SLEEC coronagraph instrument transmits 0.182 / 0.49 = 37% of the available exoplanet light from an unobscured telescope.***

Wavefront control. The deformable mirrors serve both to create the high contrast dark field and to correct for aberrations and drift in the wavefront anywhere in the optical path. Likely sources of wavefront errors in the DST optical system must be stringently controlled. Contrast sensitivities for the 70% design have been calculated for representative types of actuator noise and low-order distortions in the wavefront. For each of these cases, FALCO calculations show that the degradation in contrast ΔC increases quadratically with the rms error, with coefficients for individual errors tabulated in ***Table A1***. These are modeled as static surface distortions added to the DM (or DMs) surface after achieving the $1.3x10^{-12}$ contrast baseline. They give a rough indication of sensitivities to errors which may occur in pupil or other planes in the optical path.

Setting a fiducial goal of $3x10^{-11}$ or better for testbed instrument contrast $C+\Delta C$ leads to control requirements listed in the ***Table A1***. In the absence of any other errors, for example, the control system must stabilize DM actuator displacements within ~3.7 pm rms or better. Typical single-actuator displacement vs. voltage for the Xinetics DMs is 4 nm/volt, hence the surface requirement maps to ~0.9 millivolts rms stability once the high contrast field has been established.

Stability requirements for the Zernike terms on DM1 can be estimated from the coefficients in the table. For example, if the z2 tip/tilt term on the DM1 surface were the only significant error, then contrast of $3x10^{-11}$ or better would require z2 stability of 0.25 nm rms (0.0018 λ_0/D rms tilt or 67 nm rms lateral displacement at the f/33 focal plane) or better once the high contrast field has been established. Of course, a combination of Zernike errors appearing on the DMs (or elsewhere in the optical path) will degrade the dark-field contrast accordingly. Detailed information on surface errors and alignment drift throughput the DST optical system, which we do not have, would be required to compute global tolerances with the FALCO package.

DM surface figure error	location	ΔC coefficient	surface error to degrade contrast to 3×10^{-11}
Actuator noise (gaussian)	DM1 & DM2	2.06×10^{-6} nm^{-2}	3.7 pm rms
Tip/Tilt (z2 or z3)	DM1	4.44×10^{-10} nm^{-2}	254.0 pm rms
Focus (z4)	DM1	1.73×10^{-8} nm^{-2}	40.7 pm rms
Astigmatism (z5 or z6)	DM1	4.86×10^{-9} nm^{-2}	76.9 pm rms
Coma (z7 or z8)	DM1	1.41×10^{-7} nm^{-2}	14.3 pm rms
Trefoil (z9 or z10)	DM1	1.76×10^{-8} nm^{-2}	40.4pm rms
Spherical (z11)	DM1	6.17×10^{-7} nm^{-2}	6.8 pm rms

Table A1. Sensitivities of contrast to likely testbed wavefront errors. Contrast averaged over the 3-9 λ_0/D, 360° dark field will degrade as $C + \Delta C$, where $C = 1.3\times10^{-12}$ for the SLEEC coronagraph, and ΔC = coefficient x (rms surface error)^2.

A.1.1. The SLEEC hybrid Lyot FPM manufactured by SILIOS. The terraced circular nickel pattern is built up on the first surface of a fused silica substrate with standard lithography technology. Following deposition of the terraced nickel layers, a uniform-thickness layer of MgF_2 is vacuum deposited over the entire substrate. Substrate was manufactured by Coastline Optics using Corning grade 0-A highly-homogeneous fused silica. The first surface has no AR coating, backside has a 0.5% reflecting AR coating. The lithographic method yields sharp-edged terraced features.

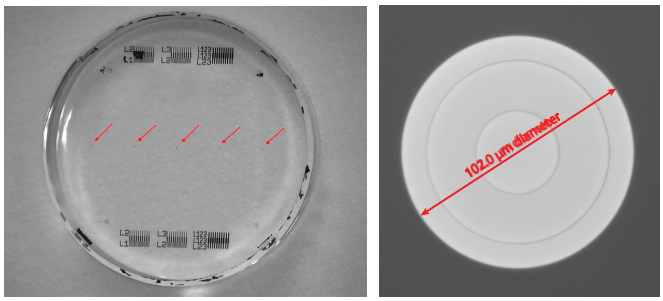

Figure A1-3. Terraced-thickness HLC masks manufactured by SILIOS (France). Five identical copies, spaced by 4 mm, have been formed on the first surface of a grade 0-A fused silica substrate. The diameter of the FPM is 102 μm, corresponding to a radius of 2.8 λ/D in an f/33 beam at 550 nm wavelength. Diameter of the FPM substrate is 25.4 mm, thickness is 6.4 mm, and AR coated on the backside.

A.1.2. The SLEEC Hybrid Lyot FPM manufactured at JPL. Two circular nickel layers superimposed on the fused silica substrate, overlayed by a uniform cryolite layer. The FPM was built up as a sequence of vacuum depositions through stencil masks in a single continuous vacuum run. The central Zernike WFS dimple is omitted here for simplicity, as not relevant for these DST tests. Dominant manufacturing error is a 2-μm off-centering between the two circular nickel patterns. FALCO model of this defect indicates that off-centering on this scale causes no significant degradation in predicted contrast. Vacuum deposition with stencil masks yields soft-edged features, modeled in FALCO as a 2-μm peak-to-valley cosine apodization.

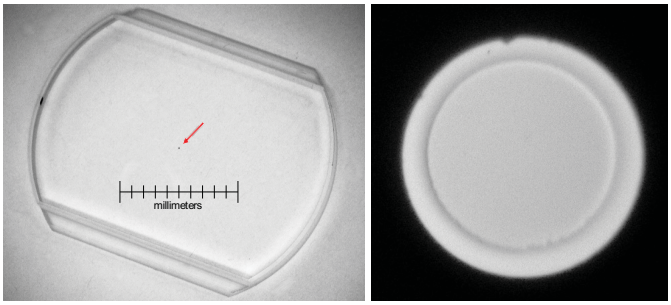

Figure A1-4. Terraced thickness focal plane mask "CM20230127" manufactured in the PI's vacuum deposition system at JPL.

A.2. The classic Lyot focal plane mask is comprised of an opaque circular occulting spot of diameter 2.8 λ_0/D on a high-quality fused silica substrate. The DST commissioning FPM was used for reference in our experiments, with the intention of establishing a baseline contrast performance consistent with the commissioning DST demonstrations by Seo et al. (S19). A second classic Lyot mask was manufactured by SILIOS on a wedged substrate, intended to test the effectiveness of a 0.8° wedge to offset internal reflections from the central optical beam. Previous calculations for the classic Lyot were performed by Dwight Moody assuming an annular Lyot stop, as used in the DST commissioning demonstrations, and as indicated in Figure A2-1. FALCO computations were carried out for these same examples of hard-edged and apodised-edge occulting spots, except with an unobscured circular Lyot stop, yielding essentially the same contrast results.

A.2.1. Classic Lyot Coronagraph (DST commissioning mask). Manufactured at JPL's Micro Devices Laboratory on 'UV grade' plane parallel fused silica substrate with a thickness of 6.4 mm. Both surfaces were AR coated prior to deposition of the circular opaque nickel occulting spot.

A.2.2. Classic Lyot FPM on a wedged substrate manufactured by SILIOS. Simple circular nickel disk on fused silica formed on the first surface by lithography. First surface has no AR coating, backside has a 0.5% reflecting AR coating. Substrate is wedged by 0.8° to offset internally reflected ghost images from the high contrast field. The wedge offsets the backside reflection such that it is separated from DST's f/32.4 main beam by 1.3 times the beam diameter. A baffle can be inserted at OAP3 to remove the internally reflected light.

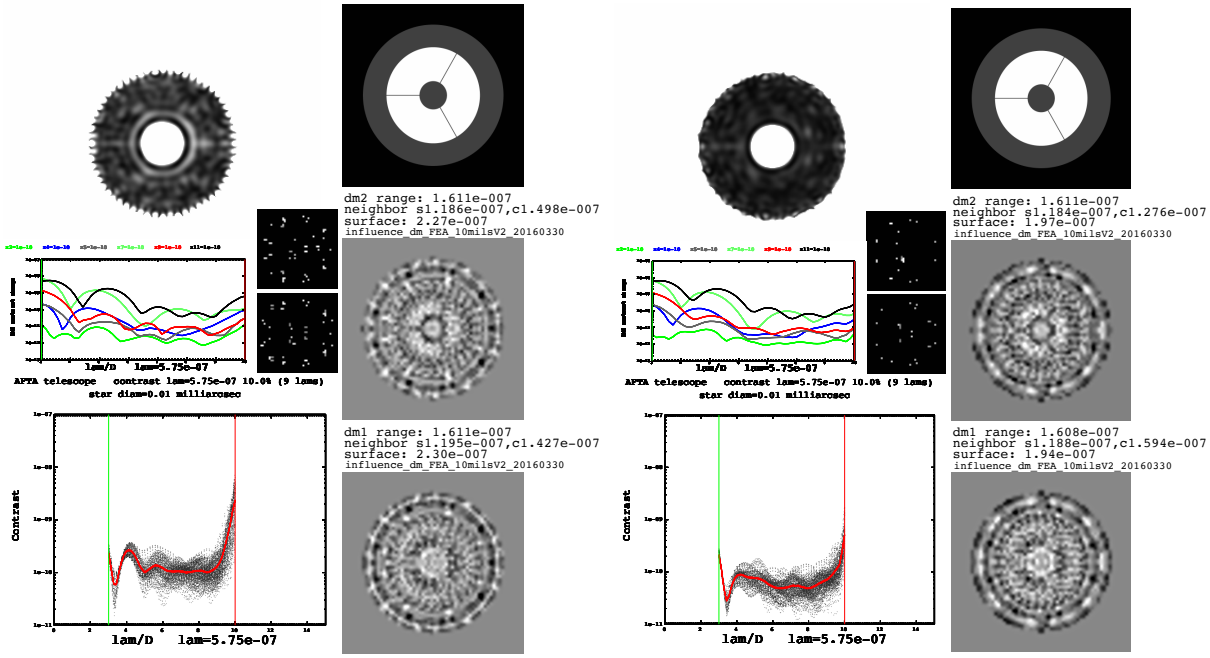

Figure A2-1. Predicted contrast for hard-edged (left) and apodized (right) Lyot coronagraph masks on the DST, computed by Dwight Moody (2020). Contrast for the hard-edged FPM averages 1.2×10^{-10} over the 3-9 λ_0/D field, and better than 10^{-10} for the apodized case. These predictions by Dwight Moody for the hard-edged FPM are in close agreement with FALCO computations for the classic Lyot coronagraph.

A.3. Particulate contamination on the FPM. The two SLEEC FPMs were inspected under the microscope in the PI's laboratory following the testbed experiments reported here, using an Olympus SMC-6 measuring microscope with 20x objective lens (0.40 NA, 0.84 μm resolution). These images are representative of the condition of the FPMs during the experiments. (Inspections at comparable magnifications were not carried out in the DST laboratory.)

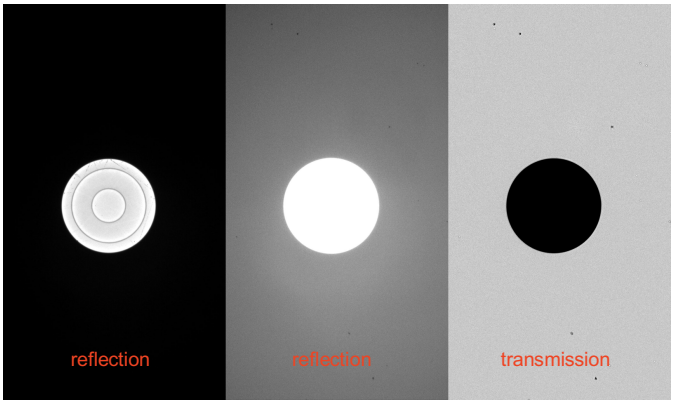

Figure A3-1. Microscope images of the SLEEC HLC mask (at center among the five masks on the substrate) in reflection, in reflection overexposed to show the particulates, and in transmission. Observed sizes of the particulates are near the 2-μm resolution limit of the microscope. Fine granularity in the images is CMOS pixel noise.

The SLEEC HLC FPM was manufactured by SILIOS. It is a circular terraced-layer nickel occulter overcoated with magnesium fluoride, as described in ***A.1.1***. The microscope image of the first surface of the FPM shows a distribution of particulates with dimensions near the resolution limit of the microscope, therefore smaller than ~2 μm. As these static features are co-planar with the occulting feature, the effects of these particulates on achievable contrast can be simulated by adding a representative particulate to the model FPM mask, then running the standard iterative FALCO optimization of the DM actuator settings. Simulations were run for a single particulate located 3.5 λ_0/D from the center, with diameters ranging from 0 to 7 μm. While the particulate initially produced, for the 5 μm case as an example, a speckle feature with peak height ~10^{-6}, an additional 30 FALCO iterations quickly reduced the background to the 1.3x10^{-12} level with no residual evidence of the particulate feature. This confirms that the probe-pair iterations easily compensate for small static defects in the focal plane mask (as was also seen for the slightly off-centered mask in Figure A1-4). As the particulates are smaller than 2 μm, the contribution to dark field contrast is negligible at the ~10^{-12} level.

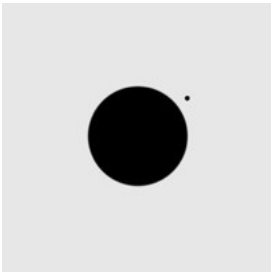

Figure A3-2. Transmittance pattern for a SLEEC FPM with the addition of a static 5μm-diameter obscuration at a radial distance of 3.5 λ_0/D. FALCO optimizations were carried out for a range of these model 'particulates' with diameters up to 7 μm. The effects on DST demonstrated contrast are negligible, as particulates on the FPM are smaller than 2-μm in size.

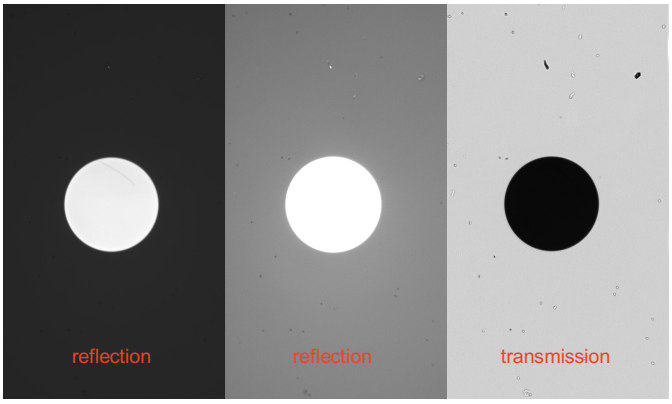

Figure A3-3. Microscope images of the classic Lyot FPM manufactured by Silios on an 0.8° wedged fused silica substrate. This mask has particulates in the 2-µm range as well as two particles in the 5-µm range. Following these measurements, we note that a brief puff of air removed the 5-µm particles, but no movement was seen in the smaller particles. As in the case of the SLEEC mask, the effects are insignificant in comparison with the predicted $1x10^{-10}$ contrast for the classic Lyot over a 10% bandwidth averaged over the dark field.

Appendix B

Potential for ghost images created by near-normal internal reflections in the DST optical path

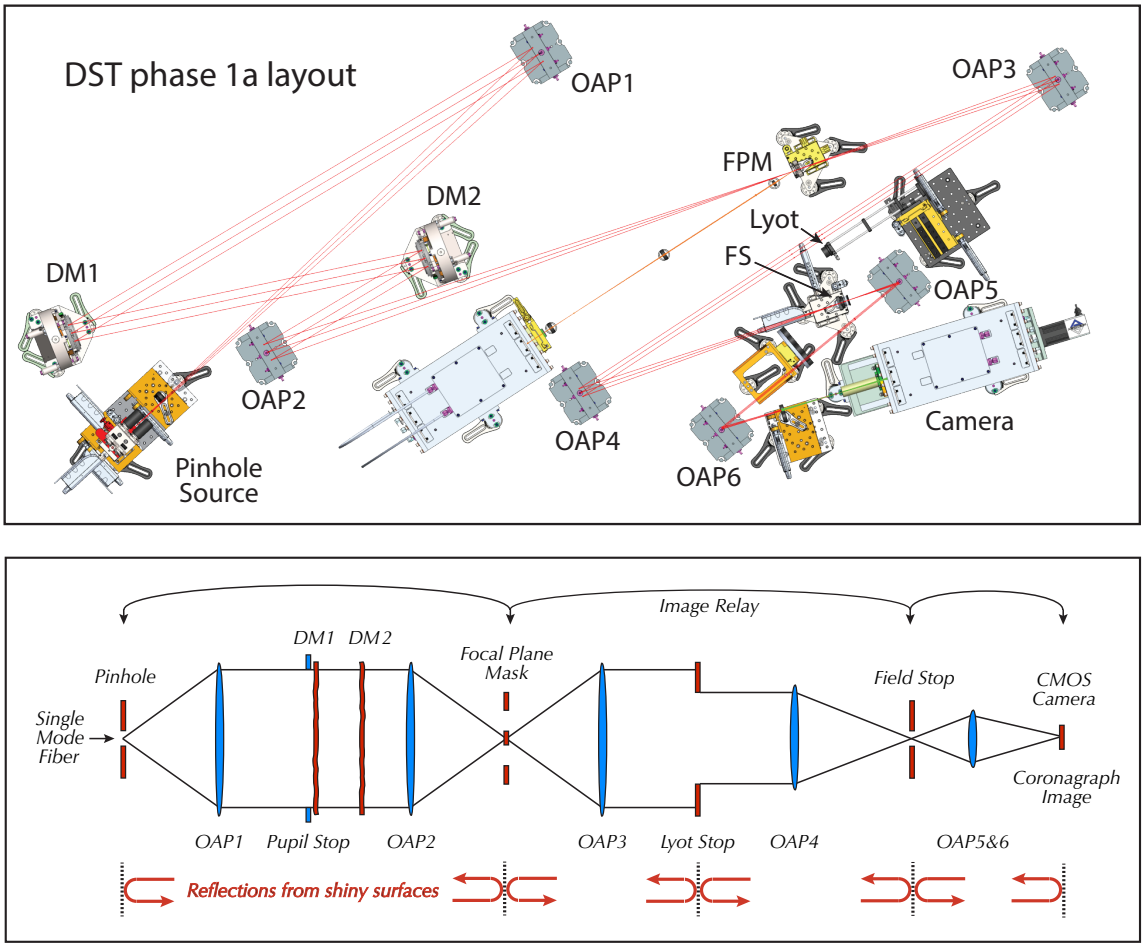

Figure B1. Potential origin of speckle-like ghost reflections. The optical layout for the SLEEC DST experiments is shown. The upper CAD graphic identifies the elements of the DST coronagraph; the lower graphic sketches the key elements of optical path unfolded for clarity. The five critical reflective surfaces are indicated by the vertical dashed lines at the bottom of the sketch, with arrows indicating reflections that are guaranteed to occur at these shiny surfaces.

DST experience suggests that ghost images created by near-normal internal reflections within the coronagraph create incoherent scattered background light that compromises the achieved testbed contrast. Each of these reflective elements can direct a focused speckle-sized feature from one focal plane to another. For example, light reflecting from the Lyot stop (formed on shiny foil with an irregular surface) can return to the FPM, where the in-focus feature can reflect from the FPM and add an incoherent feature to the coronagraph image. Or a fraction of the light at the focal plane of the CMOS camera (with scattering surfaces as detailed in ***Figure C-2***) can reflect to the field stop, then return by reflection in-focus to the CMOS focal plane. Likewise for other combinations of near-normal reflections from multiple shiny elements. Such effects are not negligible for light suppression at the 10^{-10} levels. Multiple reflections among these five elements can further confound the dark field speckle background.

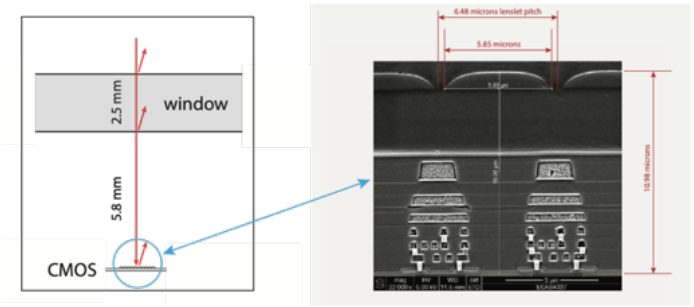

Figure B2. SEM cross section of CMOS lenslet/pixel structure (provided by Andor, April 2017). The physical structure of the Andor CMOS focal plane scatters light in multiple ways. An un-tilted plane parallel vacuum window with AR coatings (R< 0.5%, 540-750 nm) is located 5.8 mm in front of the CMOS sensor. The sensor itself comprises an AR-coated lenslet array and electrode structure that defines the pixel array with dimensions as shown. Reflections, while suppressed, may contribute ghost images that are significant at the extremely low light levels in the coronagraph dark field.

Appendix C

Experimental testbed factors with potential to limit coronagraph performance

Experimental factors critical to coronagraph testbed performance are collected here. Each of these has the potential to degrade demonstrated contrast at ~10^{-10} levels. Some have been observed and quantified in previous work, such as the DST commissioning experiments. Some can be estimated from model predictions, and a significant number of them are not well-quantified at this time, even for the DST. These factors are related to the quality of the optical elements, alignments, ghost images and stray light, and are applicable to any coronagraph configuration, whether Lyot, vortex, or other types. These factors tend to add incoherently to the total background intensity in the high-contrast dark field.

While this list is compiled specifically for the coronagraph testbed hardware, nearly all of these factors (excluding items 9 &17) are fundamental for coronagraph performance and will reappear as analogous requirements for the ultimate space coronagraph and observatory optical systems.

1. ***Ghost reflections*** from the backside of the FPM substrate. Commissioning DST demonstration with a classic Lyot FPM was estimated to contribute 1.0×10^{-10} to the dark field contrast [S19]. Remedies include: a 0.8° wedge in the substrate to separate the backside beam from the main central beam, at OAP3 to remove ghost beam from the optical system, and low-reflectance AR coating on the backside of the FPM.

2. ***Multiple internal reflections*** need to be minimized among the shiny coronagraph elements that are nearly normal to the beam in the coronagraph optical system, as illustrated for the DST in ***Figure B1***. These elements are the source pinhole, the FPM substrate, Lyot stop, field stop, and the CCD focal plane. Remedies include blackening and optimal off-axis tilts for these elements and the addition of baffles as appropriate.

3. ***Scatter by particulate contamination*** on elements near focal planes, including the FPM and optical elements near the image focal plane. Remedies include a cleanliness protocol supported by close in-situ inspection of the elements under bright light and magnification.

4. ***Line-of-sight jitter***, which was estimated to contribute dark field background at the 0.4×10^{-10} contrast level in the DST commissioning demonstration [S19]. Remedies include vibration isolation (e.g., the CCT chamber is on air legs, the coronagraph optical table is on elastomeric dampers) and isolation of sources of vibration on the optical table (such as a shutter), as verified with accelerometers in the chamber.

5. ***Chromaticity of the coronagraph elements*** over the 10% bandwidth, which was estimated to contribute 0.9×10^{-10} to the dark-field background with the classic Lyot FPM in the DST commissioning experiment [S19]. Mitigation must be a part of coronagraph design, including consideration of dispersion in the refractive index of FPM optical materials and DM surface patterns for high contrast.

6. ***Discretization at the least significant bit in the DAC*** and electrical noise in the DM driver, which was estimated to contribute 0.9×10^{-10} to the contrast in DST commissioning [S19]. Mitigations include working at a minimal DM bias voltage (reduced gain/volt due to quadratic response of AOX DMs), reduced power supply voltage to reduce the magnitude of the LSB voltage step, and adoption of a driver with more digital resolution (i.e., 20 bits rather than standard 16 bits).

7. ***Polarization and birefringence due to FPM substrate*** index inhomogeneity, which was estimated to contribute 1.2×10^{-10} to the contrast during DST commissioning [S19,24]. Mitigations include choice of highest-homogeneity/lowest birefringence substrate material (e.g., Corning class 0A fused silica) and minimum substrate thickness.

8. ***Other polarization effects*** include the cumulative polarization state created by bare-aluminum-coated OAP and tilted mirror elements, as well as inadvertent vignetting and glints from hardware in or near edges of the optical beam, as evidenced in the DST by the reduction in incoherent background (typically by a few $\times 10^{-10}$) when an analyzing polarizer is inserted near the end of the optical path.

9. ***Source pinhole irregularities***, waveguide effects, nonuniformity of pupil illumination, which was estimated to contribute up to 1×10^{-10} in DST commissioning demonstrations [S19]. Mitigations include custom pinhole fabrication at JPL's Micro Devices Laboratory, selected for best quality, such as a 4-micron diameter pinhole, waveguide effects minimized with pinhole cut into a 1-micron-thin silicon nitride material, opaque surrounding surface (200 nm thickness aluminum coated layer for opacity), illumination from single mode fiber coupler well-centered on the pinhole, uniform illumination of the entrance pupil illumination via steerable pinhole source assembly. Pinhole is a source of polarization cross terms.

10. ***Optimal FALCO EFC parameters and Tikhonov regularization schedule.*** Experimentation with the regularization schedule (balancing between overfitting and underfitting in non-linear least-squares optimization) is recommended for best achieved contrast [25]. Regularization schedules are expected to differ depending on the initial states of the wavefront prior to DM actions.

11. ***Focal Plane Mask manufacturing imperfections***. Measurement of critical characteristics as feedback for manufacturing refinements. Simplicity of hybrid Lyot FPM allows accurate measurement of key characteristics, and simplicity of design allows fabrication with a minimum of physical imperfections.

12. ***Red leak background*** in the spectrum of source illumination is a critical concern at inner working angles in the dark field. Model calculations (***Figure C1***, D. Moody 2014) lead to requirements for off-band rejection of 10^{-8} or better and a sharp red cutoff in the bandwidth-defining spectral filters. The red-leak requirements can be met with well-blocked commercial bandpass filters such as obtained from Materion. To be doubly sure the red leak is under control, two such filters can be combined in series.

13. ***Imaging sensor scattered light and pixel crosstalk.*** A CMOS camera, for example, introduces scatter from lenslets, focal plane micro-structure, and reflections from a vacuum window which have not been accurately modeled. A back illuminated CCD may be preferable for minimal scatter and crosstalk. CCT utilizes a TEC-cooled, back-illuminated e2V CCD packaged together with its low-noise electronics in a vacuum compatible enclosure.

14. ***Minimum number of transmissive optics*** in the highly corrected beam upstream of the focal plane mask. Transmissive elements introduce dispersion in refractive index, birefringence, scatter, and ghost reflections. The hybrid Lyot coronagraph has only one transmissive element, the FPM, which can be AR coated and made of highest homogeneity fused silica.

15. ***DM actuator creep and temperature sensitivity*** are well-known characteristics of the PMN electrostrictive actuators, as observed with AOX DMs and Gen5 electronics drivers. Creep on time scales shorter than experiment times may degrade performance. Mitigations include ring-in sequences when changing voltage settings, minimization of large voltage swings, maintenance of continuous power to the DM. Thermal control on mounts and electronic interconnect cables are essential, as well as a temperature-controlled DM enclosure to restrict DM's view of ambient surroundings in the vacuum.

16. ***Low-order aberrations due to alignment drift*** calls for stable mounting hardware, temperature regulation in the testbed laboratory, and closed loop temperature control of the critical active optics (DM, tilt stage).

17. ***Ambient air turbulence.*** Operate in vacuum chamber (e.g., Exoplanet Imaging Technology Laboratory turbo-pumped vacuum chamber operates at ~$3x10^{-7}$ torr).

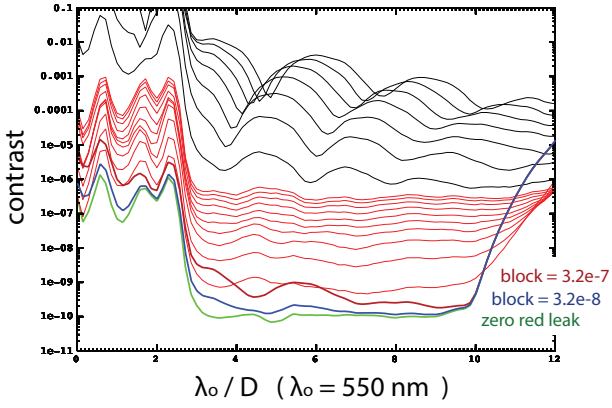

CWL	BW	Filter	CCD
550.0	10	1	0.95
580.3	1	1.80E-02	0.96
586.1	1	4.00E-04	0.95
591.9	1	4.80E-05	0.95
597.7	1	7.50E-06	0.94
603.4	1	1.10E-06	0.94
609.2	1	block	0.94
615.0	1	block	0.93
620.8	1	block	0.93
626.5	1	block	0.92
632.3	1	block	0.91
664.1	10	block	0.90
721.8	10	block	0.84
779.6	10	block	0.73
837.3	10	block	0.61
895.1	10	block	0.44
952.8	10	block	0.28
1010.6	10	block	0.10

Figure C1. Contrast degradation due to filter red leak (see Item 12) for a classic Lyot coronagraph. Contrast performance requires strong light suppression at wavelengths shortward and longward of the nominal 10% bandwidth, a requirement that is independent of the specific coronagraph architecture. The figure shows the incremental effects of leakage within individual wavelength intervals longward of the 10% bandwidth. Table at right defines a contiguous set of wavelength intervals covering the spectrum from 550 to 1010 nm, with filter transmittances and silicon CCD detector QEs averaged over each interval. Filter transmittance longward of 609 nm is taken to be $3.2x10^{-7}$, $3.2x10^{-8}$, or zero as indicated. The curves plotted at left show, top to bottom, the achievable contrast as each interval of blocking is added. We rely on a well-blocked interference filter with out-of-band blocking better than 10^{-8} for contrast performance of 10^{-10} or better.

Appendix D

Progress towards global optimization of the SLEEC design (P. Chen)

Global optimization based on conventional brute-force methods is impractical, even with highly efficient optical propagation routines and parallel computing. A major challenge lies in the dimensionality of the computational problem. For instance, a pair of DMs alone (each with 48 actuators across the diameter) constitutes a 3620-dimensional optimization problem. We developed a new software for global design optimization to meet this challenge. By global, we mean that the software simultaneous explores combinations of parameter values (we will refer to each combination as a state) in four coronagraph planes—DM1, DM2, FPM, and Lyot-stop—returning a likelihood based on required exposure time for each state. The objective of this software algorithm is not to attain the ultimate contrast performance on its own; rather, it is to identify promising regions in design-parameter space that can be subsequently mined by a conventional, gradient-guided algorithm (e.g. Levenberg-Marquardt) to obtain deep contrast. Implementing such a software required a set of innovations to handle the parameter space's extraordinarily large dimensionality; for example, suppressing starlight to create a 10 λ/D radius dark hole can require thousands of parameters, mostly in DM actuator settings. We introduced the following innovations that work together to solve the dimensionality problem:

- ***Markov-chain Monte Carlo (MCMC) optimization methodology.*** Although MCMC is well established in Bayesian retrieval of physical states from measurement data, its application in optimization is still unconventional. We refer the reader to Hobson & Baldwin (2004) as a rare, yet highly relevant, reference describing an MCMC application to optical design optimization. MCMC offers the following advantages:
  - It is not a gradient-based or linearized approach. As such, it is robust with respect to trapping in local optima and nonlinearity. Local trapping and slow convergence due to nonlinearity are well known issues in coronagraph optimization.
  - Compared to grid sampling, MCMC is far more efficient in sampling large parameter space. Instead of uniform sampling, MCMC samples parameter space according to the joint probability of a likelihood PDF (probability distribution function) and PDFs of prior parameter values. The likelihood function is analogous to the merit function in conventional optimization algorithms. Well formulated likelihood function (see below) and prior functions concentrate exploration of interesting regions in parameter space.
  - One can store the full record of sampled states and their associated coronagraph design and performance parameters. This enables identification of multiple families of solutions offering similar performance, identifications of correlations between design parameters, and analyses to trade, e.g., design against performance factors.
- ***Parallel sampling algorithm.*** Myriad sampling algorithms exist to implement MCMC, many of them have limitations with respect to parallel computing. Due to the high dimensionality, parallelization is essential for our application. We adopted the affine-invariant ensemble sampler (Goodman & Weare 2010), as implemented in the open-source EMCEE Python package (Foreman-Mackey et al. 2013). This algorithm scales as an "embarrassingly-parallelizable problem."
- ***Optimal basis set.*** The high dimensionality of the coronagraph optimization problem demands more than just parallel computing. Model-order reduction (MOR) is another key method to enhance computational speed. The choice of a mathematical basis set to most efficiently represent complex (real & imaginary) amplitudes at key optical planes. Here, efficiency implies representing significant optical changes with the fewest number of modes. Commonly utilized basis sets have inherent limitations. For example, the 2-D Fourier basis is not orthonormal over finite domains, such as the domain of pupil. Zernike polynomials are orthonormal over the circular domain (useful for circular pupils). However, they are derived with either zero-amplitude or zero-derivative (Dirichlet or Neumann) boundary conditions, which do not necessarily represent the physical system at hand (e.g. DM surface solutions), and they are not appropriate for non-circular geometries (e.g. an assembly of hexagonal mirror segments forming a primary mirror). We have identified prolate spheroidal wave functions (PSWFs) as an optimal basis set. PSWFs are solutions of the energy-concentration eigenvalue problem [e.g. Slepian 1964]. In optical terms, the problem poses the question: What function will concentrate the most energy in both Fourier conjugate domains (e.g. spatial and spatial-frequency domains or pupil and focal planes)? The eigenvalue of each PSWF mode corresponds to encircled energy in Fourier space. In coronagraphic terms, applying a PSWF at a pupil will optimally concentrate light intensity inside a target zone in the focal plane; if the target zone is an occulting mask, the PSWF is the optimal pupil apodization for starlight suppression. In fact, this is the basic principle of the apodized-pupil Lyot coronagraph (APLC, e.g. Soummer et al. 2009). As such, PSWFs comprise modes that are inherently ranked by their effect on starlight suppression. Aside from orthonormality over arbitrary finite domains and energy concentration, PSWFs also have the unique property that each mode has the same shape in both Fourier domains, analogous to the Gaussian function. These unique properties are very useful for efficient representations in coronagraphic problems. In a test case optimizing DM surfaces vis-à-vis the Roman Space Telescope (RST) pupil, we found that using 9 PSWF modes achieved the same contrast level as using 2000 Fourier modes, *reducing computation time by a factor of ~200*. However, pre-existing algorithms computed PSWFs for 1-D, circular, and spherical domains, and most numerical techniques broke down for high order modes, which can be important for coronagraphy. The article by Co-I Chen and colleagues at Howard University (Yan et al. 2022) reports a new algorithm using the method of moments to solve for PSWFs for arbitrary geometry and arbitrarily high orders. ***Figure D1*** shows the 24 PSWF modes derived from the LUVOIR-A aperture geometry.

Other notable features of this software include the following:

- ***Science-traceable merit function:*** Instead of using only contrast and throughput as the merit function, we use required exposure time to reach a target SNR as the likelihood function. Based on Equations 7 – 15 in Stark et al. (2014), the likelihood function accounts for coronagraphic parameters such as contrast, throughput, and PSF footprint, as well as astrophysical parameters such as zodiacal brightness.
- ***Open-source codes***: The software uses HciPy (Por et al. 2018) for Fresnel propagation and EMCEE (Foreman-Mackey et al. 2013) for MCMC computations, both of which are open-source Python software. We plan to release our software open source as well.

One example application of the software was finding DM surface solutions at ~$2\text{x}10^{-6}$ contrast level (3.5 – 6 λ/D, 10% bandwidth) using the RST Coronagraph Instrument (CGI) configuration. As stated above, the purpose was not to reach the ultimate contrast; rather, it was to identify multiple families of DM solutions and to confirm that solutions from gradient-based optimization were not trapped in local optima.

In the future, we would like to integrate the global algorithm with a gradient-guided algorithm to enable end-to-end optimization of coronagraph designs with high dimensionality.

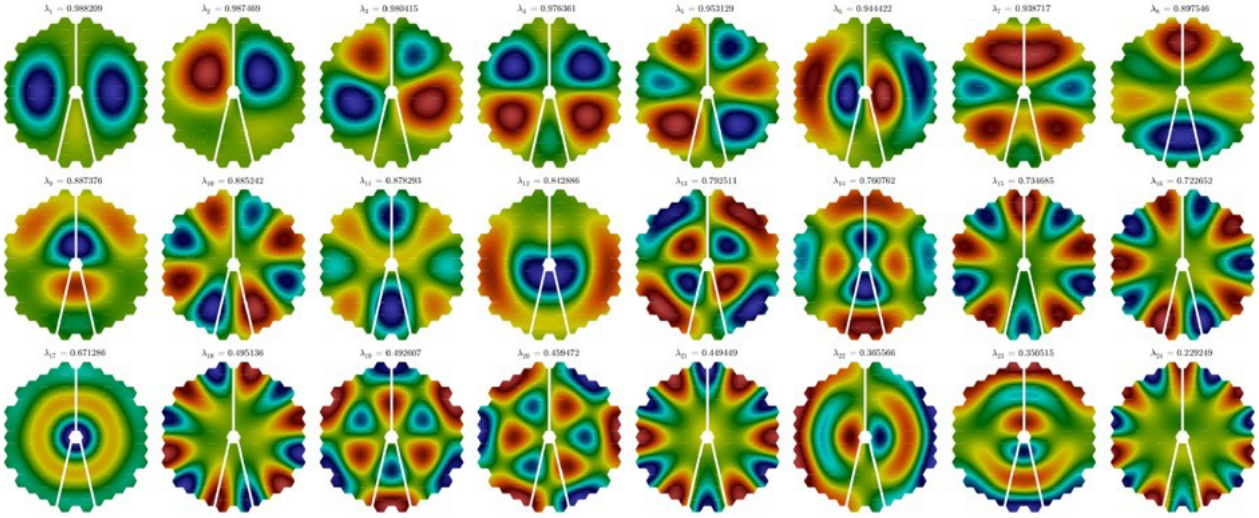

Figure D1. First 24 PSWF eigenmodes supported by the LUVOIR-A aperture (Yan et al. 2022).

In the rest of this section, we present results demonstrating our algorithm's distinguishing capabilities as an engine for global exploration of design spaces.

Demonstration setup. First, we describe how we set up the chosen demonstration MCMC run to identify optimal design regions for a coronagraph with a clear, circular aperture, a pupil apodizer (amplitude only), two DMs, a circular FPM, and a circular Lyot stop. The run evolved coronagraph states comprising the following variables specifying the coronagraph's four key optical planes:

- Pupil: 3 coefficients for a basis set of 3 PSWFs corresponding to N2D values (Simons & Wang 2011) of 10, 15, and 22. The pupil amplitude transmission function is a linear combination of the basis functions with the given coefficients. These coefficients are denoted as θ_1, θ_2, and θ_3.
- DM1: 3 coefficients for a basis set of 3 (Bessel) disk harmonics (J_n) corresponding to n = 1, 2, and 3. The DM surface is a linear combination of the basis functions with the given coefficients. These coefficients are denoted as θ_4, θ_5, and θ_6.
- DM2: 2 coefficients for a basis set of 2 (Bessel) disk harmonics (J_n) corresponding to n = 2, and 3. The DM2 surface is the opposite shape of DM1 plus a linear combination of the basis functions with the given coefficients. These coefficients are denoted as θ_7 and θ_8.
- FPM: diameter of the opaque circular focal plane mask, denoted as θ_9.
- Lyot stop: diameter of the circular Lyot aperture, denoted as θ_{10}.

The MCMC run utilized 40 walkers (i.e., numerical particles with evolving states) that evolved over 2913 iterations, thus sampling a total of 116520 states. The likelihood function has the following form:

$$\sum_k e^{-\left(\frac{\tau_k - \tau_{target}}{\tau_{tol}}\right)^2}$$

Here, τ_k denotes the required exposure time (Equation 7 in Stark et al. 2014) in the k^{th} annular λ/D band; τ_{target} and τ_{tol} denote user-prescribed target exposure-time and exposure-time "tolerance" values. For the herein discussed run, we used $\tau_{target} = 0$ and $\tau_{tol} = 20$ hours.

The MCMC samples by rejection. After a burn-in period, the density of sample occurrences reflects the probability density function that is the product of the likelihood and (user prescribed) prior probability functions (PDFs) for the state variables. For brevity, we do not present the input prior functions for the 10 variables of this run, except to say that they are uniform PDFs over intervals that bracket reasonable ranges of possible values.

Demo Run Results. The evolution of ln(probability) vs. iteration for all 40 walkers is shown in ***Figure D2*** below. Notable features include the following:

- The probability value increases initially and reaches two plateaus after ~2200 iterations.
- The bifurcation (two plateaus) after ~2200 iterations indicates a global optimum (with the highest ln (probability value) and a secondary, local optimum.

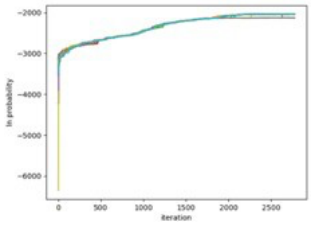

Figure D2. Ln(probability) vs. MCMC iteration for all 40 walkers.

Figure D3 shows a corner plot of the run results. Recall that higher sample density corresponds to higher probability, which corresponds to more optimal design states (i.e. shorter required exposure time enabled by variable values within the prior ranges). Two general aspects are especially noteworthy:

- ***Correlated variables***. { θ_1, θ_2, θ_3}, which define the pupil apodization, form a set of linearly correlated variables, as indicated by the almost linear contours of the covariances between all pairings of these variables. One should be able to reduce these three variables into one by constructing a linear combination of the three using coefficients derived from the slope of covariance. Another such set is { θ_4, θ_5, θ_6}, which define DM1's surface figure.
- ***Multiple optima.*** The FPM diameter (θ_9) and the Lyot stop diameter (θ_{10}) each show two distinct regions of high probability. Moreover, examination of the corner plot's bottom row, which plots ln(probability) vs. variable values, also show two distinct regions of high probability for each of these two variables. These signs and the bifurcation in ***Figure D3*** all point to the existence of a primary, global and a secondary, local optima in design space. The dual optima reveal a design trade; a smaller FPM diameter tends to degrade contrast (and improve inner working angle), and making the Lyot stop smaller can compensate to some extent.

We subsequently continue the run to 10000 iterations, which showed the same, persistent bifurcation until ~ 9800 iterations, after which all walkers converged into the global optimum.

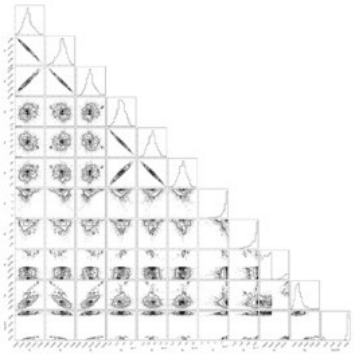

Figure D3. Corner plot

Samples with the highest probability scores show the following characteristics: average contrast in the 2.5 – 5.5 λ/D, annular dark zone = 2.3 x 10^{-10} and core throughput = 13% in monochromatic light

Figures D4 and D5 show the pupil and DM optical planes and contrast map associated with this state.

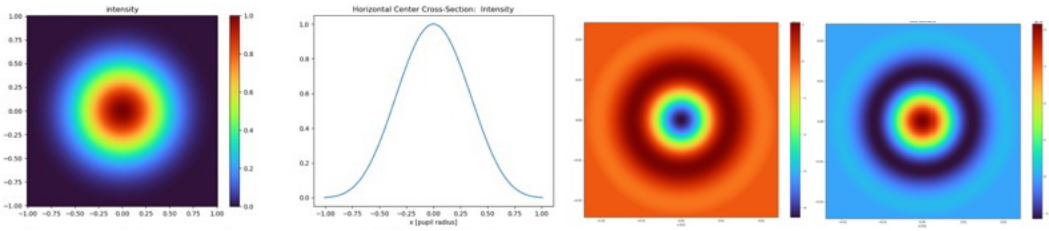

Figure D4. From left to right: contour plot of pupil transmission intensity function; center crosscut of the pupil transmission function, DM1 surface height, and DM2 surface height.

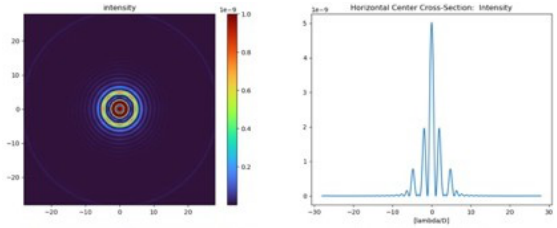

Figure D5. Contrast

In summary, the preliminary demonstration evidenced our algorithm's capability to efficiently explore design-parameter space and reveal multiple optima and parameter correlations. These capabilities should inform design trades, enable model-order reduction, and provide optimal initialization of gradient-guided design algorithms.

Next Steps. The logical next steps to advance this work include the following major elements:

- Combine the method-of-moments algorithm described in Yan et al. (2022) and the MCMC algorithm to enable global optimization for arbitrary pupil geometries (e.g. those of HWO EACs)
- Develop an algorithm to translate MCMC findings into initial states for gradient-guided algorithms such as FALCO.
- Conduct end-to-end (global to gradient-guide) design.

References for Appendix D

D. Foreman-Mackey et al. 2013. "emcee: the MCMC hammer." P.A.S.P. 125, 306. doi:10.1086/670067.

J. Goodman and J. Weare 2010. "Ensemble sampler with affine invariance." Comm App. Math. & Comp. Sci. 5, 65. doi: 10.2140/camcos.2010.5.65.

M. Hobson and J. Baldwin 2004. "Markov-chain Monte Carlo approach to the design of multilayer thin-film optical coatings." Appl. Opt. 43, 2651. doi:10.1364/AO.43.002651.

E. Por et al. 2018. "High Contrast Imaging for Python (HCIPy): an open-source adaptive optics and coronagraph simulator." Proc SPIE 1070342. doi:10.1117/12.2314407.

F. Simons and D. Wang 2011. "Spatiospectral concentration in the Cartesian plane." Int. J. Geomath 2,1. doi:10.1007/s13137-011-0016-z.

D. Slepian 1964. "Prolate Spheroidal Wave Functions, Fourier Analysis and Uncertainty-IV: Extensions to Many Dimensions; Generalized Prolate Spheroidal Functions." Bell System Technical Journal, 3009. doi:/10.1002/j.1538-7305.1964.tb01037.x

R. Soummer et al. 2009. "Apodized pupil lyot coronagraphs for arbitrary apertures. II. Theoretical properties and application to extremely large telescopes." Ap. J. 695, 695. doi:10.1088/0004-637X/695/1/695.

C. Stark et al. 2014. "Maximizing the exoearth candidate yield from a future direct imaging mission." Ap. J. 795, 1. doi:10.1088/0004-637X/795/2/122.

S. Yan, P. Chen. M. Wade, T. Gill 2022. "Optimal pupil basis set for telescope-coronagraph design and perturbation analysis based on the method of moments." JOSA 39, 2422. doi:10.1364/JOSAA.472995